

Strain-tunable topological antiferromagnetism of two-dimensional magnets with negative Poisson ratio

Yingmei Zhu,^{1,2} Qirui Cui,^{2,3,4} Bo Liu,^{1,*} Tiejun Zhou^{1,5,†} and Hongxin Yang^{2,3,‡}


¹Key Laboratory of Spintronics Materials, Devices and Systems of Zhejiang Province, Hangzhou 311305, China

²Ningbo Institute of Materials Technology and Engineering, Chinese Academy of Sciences, Ningbo 315201, China

³National Laboratory of Solid State Microstructures, School of Physics, Collaborative Innovation Center of Advanced Microstructures, Nanjing University, Nanjing 210093, China

⁴State Key Laboratory of Superlattices and Microstructures, Institute of Semiconductors, Chinese Academy of Sciences, Beijing 100083, China

⁵School of Electronics and Information Engineering, Hangzhou Dianzi University, Hangzhou, Zhejiang 310018, China

 (Received 23 August 2023; revised 7 October 2023; accepted 12 October 2023; published 30 October 2023)

Two-dimensional materials with a negative Poisson ratio, which exhibit unique mechanical behavior that expands laterally when stretched, have attracted considerable attention for their practical applications in sensors, biomedicine, and other fields. Here, using the elastic solid theory and first-principles calculations, we screen out a series of two-dimensional (2D) auxetic magnets MX_2 protected by $P\bar{4}m2$ crystal symmetry. We show that various types of chiral antiferromagnetic spin configurations can be achieved. Specifically, the elliptical antiferromagnetic antiskyrmion can be stabilized in MnI_2 and $CoCl_2$ monolayers under the external strain along the x -direction due to the coexistence of a negative Poisson ratio and anisotropic Dzyaloshinskii-Moriya interaction. Our work thus enriches the family of 2D auxetic magnets by introducing intrinsic long-range magnetic order, and it provides a platform for investigating strain-tunable topological antiferromagnetism.

DOI: [10.1103/PhysRevB.108.134438](https://doi.org/10.1103/PhysRevB.108.134438)

I. INTRODUCTION

As a fundamental mechanical property, Poisson's ratio (ν) is defined as the ratio of longitudinal strain to transverse strain. It characterizes the lattice behavior in the y -direction of materials when uniaxial strain is applied along the x -direction, which sets a range of $-1 < \nu < 0.5$ based on classical elasticity theory [1]. Different from materials with a positive Poisson ratio (PPR), materials with a negative Poisson ratio (NPR), also known as auxetic materials, exhibit untrivial mechanical properties that are laterally expanded upon stretching [2]. This feature facilitates the application of these materials in sensors [3], fasteners [4], and biomedicine [5]. Most of the reported materials with the NPR effect are contained in crystals, molecules, and network structures [6–9]. Recently, two-dimensional (2D) auxetic materials have attracted attention due to their geometric effect, such as penta-graphene, SiO_2 and SnO_2 monolayers protected by $P\bar{4}m2$, single-layer black phosphorus, and $P4mm$ -type MX ($M = Cr, Cu, Ag$; $X = Se, Cl, Br, I$) with a buckled structure [10–14]. The auxetic effect in these 2D materials has been proven based on theoretically calculated elastic constants C_{ij} and confirmed by fitting the $y-x$ -strain curve. However, systems that combine NPR and intrinsic magnetism have rarely been reported on as far as we know. On the other hand, topological magnetic quasiparticles in magnets, such as skyrmions and bimerons, have

attracted extensive research interest due to their promising applications in information storage and logic devices [15–17]. In particular, the magnetic moments and topological charge of coupled sublattices cancel out in antiferromagnets, resulting in zero dipolar field, zero skyrmion Hall angle, and high stability and mobility of topological quasiparticles [18,19]. Using x-ray photoemission electron microscopy and spin-polarized scanning tunneling microscopy, antiferromagnetic topological quasiparticles were demonstrated based on the skyrmion Hall effect in the system [20–22]. In most situations, such as an asymmetric exchange interaction induced by spin-orbit coupling (SOC), these chiral quasiparticles are mainly due to the Dzyaloshinskii-Moriya interaction (DMI), obtained in inversion symmetry-broken systems [23–25].

In this work, we use the Computational 2D Materials Database C2DB [26,27] to screen out 23 2D magnets MX_2 (where M denotes a 3d transition metal, and X denotes a VI-A or VII-A element) with $P\bar{4}m2$ crystal symmetry [28], and we calculate the mechanical properties, including Young's modulus and Poisson's ratio, via the elastic solid theory. We find that MnA_2 ($A = Cl, Br, I$) monolayers, which exhibit hybridization between 3d-orbitals from metal atoms and p -orbitals from nonmagnetic atoms, are mechanically stable and possess auxetic behavior. Moreover, the strain-tunable anisotropic DMI is obtained in those 2D auxetic antiferromagnets. The competition between various magnetic parameters leads to the emergence of antiferromagnetic antiskyrmions, and thanks to the large NPR, elliptical antiferromagnetic antiskyrmions are further induced by a uniaxial strain in those 2D auxetic materials.

*liubo@spinlab.cn

†zhoutiejun@spinlab.cn

‡hongxin.yang@nju.edu.cn

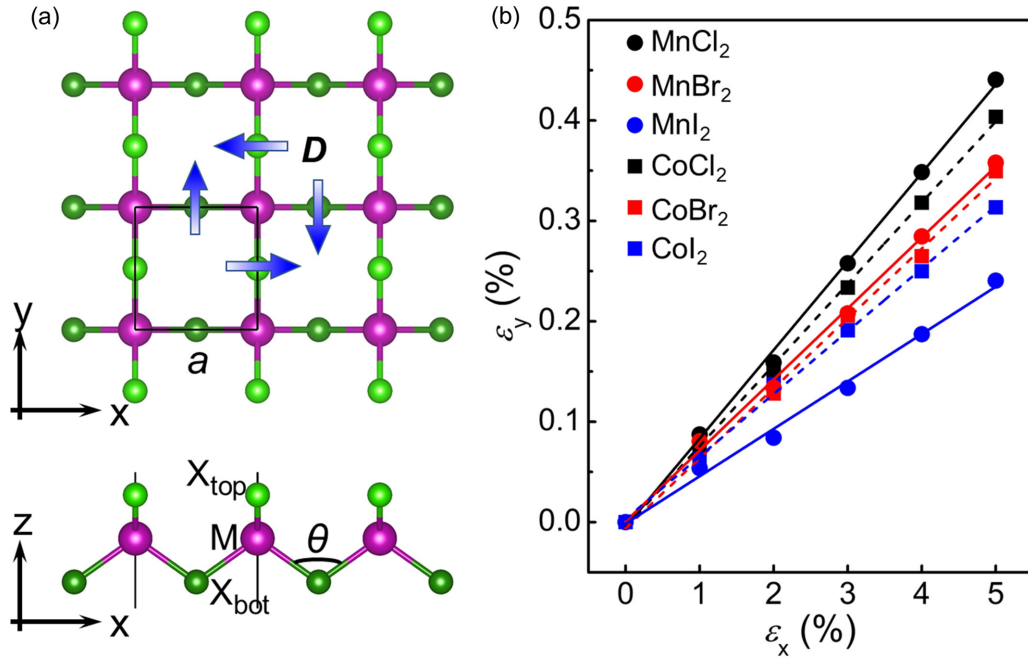


FIG. 1. (a) Top and side views of MX_2 monolayer. Purple and light-/dark-green balls represent M and X elements, respectively. (b) Mechanical properties of $MnCl_2$, $MnBr_2$, MnI_2 , $CoCl_2$, $CoBr_2$, and CoI_2 monolayers. The tensile strain along the x -axis leads to auxetic performance in the y direction. The lines indicate a linear relationship between ϵ_x and ϵ_y .

II. COMPUTATIONAL DETAILS

Our first-principles calculations are performed using the density functional theory (DFT) with the projector-augmented wave (PAW) method as implemented in the Vienna *Ab Initio* Simulation Package (VASP) [29–32]. The exchange and correlation functions are treated by the generalized gradient approximation (GGA) of the Perdew-Burke-Ernzerhof functional (PBE) [33,34]. A plane-wave cutoff energy is set to 420 eV. The GGA+ U method with $U_{\text{eff}} = 3$ eV is applied to describe the strongly correlated $3d$ electrons. The thickness of a vacuum layer is set to no less than 15 \AA along the z direction to avoid interactions between adjacent layers. The Brillouin zone is sampled using a Γ -centered $30 \times 30 \times 1$ Monkhorst-pack k -point mesh. Electronic convergence is performed with a tolerance of 10^{-7} eV. Optimized structures are fully relaxed until the force converged on each atom is less than 10^{-3} eV/ \AA . To check the dynamic and thermal stability of the auxetic materials MnA_2 and CoA_2 ($A = \text{Cl, Br, I}$) monolayers, phonon dispersions and *ab initio* molecular dynamics (AIMD) are simulated [35,36]. We adopt the chirality-dependent energy difference approach and the qSO method to obtain the DMI of the systems with the NPR effect [37–39]. The calculation details regarding the magnetic parameters are discussed in the Appendix.

III. RESULTS AND DISCUSSION

A. Geometrical stability and mechanical properties

Figure 1(a) shows the crystal structure of an MX_2 monolayer, which is constructed by one $3d$ transition-metal atom (M) and four halogen or chalcogen elements (X). As discussed in Ref. [28], the layer of MX_2 lacks inversion symmetry with

the $P\bar{4}m2$ space group and tetragonal lattice. The bending directions of $M - X_{\text{top}} - M$ and $M - X_{\text{bot}} - M$ are along the y - and x -axis, respectively. To evaluate the effect of lattice distortion on structural stability, the mechanical properties of the MX_2 monolayer are investigated based on elastic solid theory. Using the standard Voigt notation [6], the elastic strain energy per unit area for these 2D system can be expressed as

$$E_s = \frac{1}{2}C_{11}\epsilon_x^2 + \frac{1}{2}C_{22}\epsilon_y^2 + C_{12}\epsilon_x\epsilon_y + 2C_{66}\epsilon_{xy}^2, \quad (1)$$

where the coefficients C_{11} , C_{22} , C_{12} , and C_{66} are the components of the elastic tensor, and uniaxial strain in the x (y) direction and the shear strain are represented by ϵ_x (ϵ_y) and ϵ_{xy} . For a mechanically stable structure, the elastic constants should satisfy $C_{11}C_{22} - C_{12}^2 > 0$ and $C_{66} > 0$. Moreover, the in-plane Young's modulus can be obtained by $Y = (C_{11}C_{12} - C_{12}^2)/C_{22}$. The results on the elastic constants of the MX_2 family are shown in Table I. In this family system, C_{11} is always equal to C_{22} , and therefore $C_{11} > |C_{12}|$ and $C_{66} > 0$ should be satisfied. From the calculated constants, we find that the mechanical properties of MX_2 monolayers are stable except for VO_2 , CrI_2 , and FeS_2 . Young's moduli of the oxide materials, including CrO_2 , FeO_2 , and CoO_2 , are 75.586, 77.821, and 71.255 N/m, respectively, which are larger than that of traditional materials, such as silicene, germanene, and stanene [40–42]. Notably, the negative C_{12} for MnA_2 and CoA_2 ($A = \text{Cl, Br, I}$) reminds us of the NPR effect in which $\nu = \frac{C_{12}}{C_{22}} < 0$ can be found in those monolayers. Most materials have a positive Poisson ratio ranging from 0 to 0.5, while MnA_2 and CoA_2 are NPR, being similar to that of the computed SnO_2 ($\nu = -0.11$) [25], but larger than those non-magnetic materials [9,10]. To further confirm the existence of NPR in CoA_2 and MnA_2 , we calculate the responses in

TABLE I. The calculated elastic constants C_{ij} , Young's modulus, and Poisson's ratio of the MX_2 family. The units of C_{ij} and Young's modulus are N/m.

MX_2	C_{11}	C_{22}	C_{12}	C_{66}	Young's modulus	Poisson's ratio
VO ₂	77.700	77.700	5.697	-11.671	77.282	0.073
VS ₂	32.948	32.948	5.574	5.451	32.005	0.169
VSe ₂	19.385	19.385	5.770	3.600	17.668	0.298
CrO ₂	77.578	77.578	12.432	5.514	75.586	0.160
CrS ₂	22.102	22.102	2.543	2.606	21.809	0.115
CrSe ₂	13.104	13.104	1.874	1.489	12.836	0.143
CrI ₂	15.068	15.068	3.221	-21.591	14.379	0.214
MnCl ₂	17.761	17.761	-1.529	0.732	17.629	-0.086
MnBr ₂	16.891	16.891	-1.128	0.641	16.816	-0.068
MnI ₂	15.760	15.760	-0.750	0.810	15.724	-0.048
FeO ₂	79.184	79.184	10.390	12.510	77.821	0.131
FeS ₂	-15.289	-15.289	29.679	-0.521	42.324	-1.941
FeCl ₂	18.979	18.979	0.142	1.937	19.978	0.007
FeBr ₂	16.019	16.019	1.976	1.698	15.775	0.123
FeI ₂	14.500	14.500	2.639	1.691	14.020	0.182
CoO ₂	71.349	71.349	2.584	10.419	71.255	0.036
CoCl ₂	26.174	26.174	-2.192	1.279	25.990	-0.084
CoBr ₂	24.394	24.394	-1.789	1.180	24.263	-0.073
CoI ₂	22.297	22.297	-1.430	1.264	22.205	-0.064
NiCl ₂	36.021	36.021	-0.851	0.617	36.001	-0.024
NiBr ₂	32.626	32.626	-0.224	0.744	32.624	-0.007
NiI ₂	27.986	27.986	1.173	1.177	27.937	0.042

the y direction when the lattice is subjected to 0–5 % tensile strain in the x direction. Poisson's ratio, ν , is defined as the slope of the ε_y - ε_x curve, i.e., $\nu = -\frac{\varepsilon_y}{\varepsilon_x}$. As shown in Fig. 1(b), the in-plane NPR of MnCl₂ (CoCl₂), MnBr₂ (CoBr₂), and MnI₂ (CoI₂) are -0.086 (-0.084), -0.067 (-0.073), and -0.048 (-0.064), respectively. The negative values mean that the equilibrium lattice becomes auxetic perpendicular to the applied strain, which is in agreement with that obtained from elastic solid theory.

To clarify the mechanism of NPR for MnA₂ and CoA₂, we select MnCl₂ and CoCl₂ with strong NPR and FeI₂ with strong PPR for a comparison, and we explore their electronic structures. The magnetic atoms in MnCl₂ and FeI₂ monolayers are in a Néel antiferromagnetic configuration, where the magnetism originates from partially occupied $3d$ orbitals. In

a tetrahedral crystal structure, fivefold-degenerate $3d$ orbitals of M atoms split into two sets: t_2 (d_{xy} , d_{xz} , d_{yz}) and e ($d_{x^2-y^2}$, d_{z^2}). We plot the projected density of states of $M - 3d$ and $A-p$ orbitals. From Figs. 2(a) and 2(b), the similar DOS-peak shape and position between Mn(Co)- e and Cl- p orbitals near the Fermi level indicate a strong orbital interaction of metal and nonmagnetic atoms. For the DOS of an FeI₂ monolayer, the $e-p$ orbital coupling is obviously weaker than the MnCl₂ and CoCl₂ monolayers in the $[-1, 0]$ energy range (see Appendix 1). The geometric evolution of MnCl₂ (CoCl₂) and FeI₂ under uniaxial strain using the alternate corners of a cube is shown in Fig. 2(c) and Appendix 1. For MnCl₂ and CoCl₂, when the bottom two atoms are stretched along the x direction, a compressive force will appear in the z direction due to the strong $e-p$ orbital coupling, and then the M atom moves

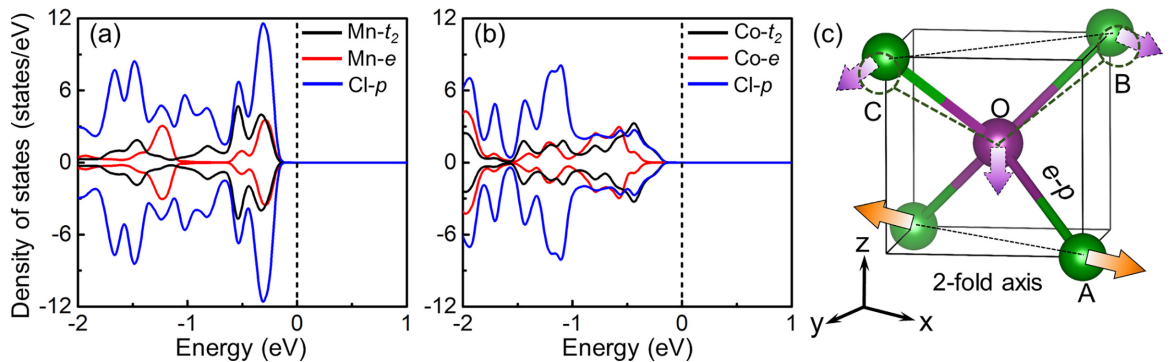


FIG. 2. Atom-projected density of states for (a) MnCl₂ and (b) CoCl₂. (c) Schematic diagram of the geometric evolution for MnCl₂ and CoCl₂ monolayers. Black, red, and blue lines represent the t_2 (d_{xy} , d_{xz} , d_{yz}) and e ($d_{x^2-y^2}$, d_{z^2}) orbitals of metal atoms and p -orbitals of nonmagnetic elements, respectively. Purple arrows in (c) indicate the resulting movement of the A_{top} atom under a tensile strain along the x -axis.

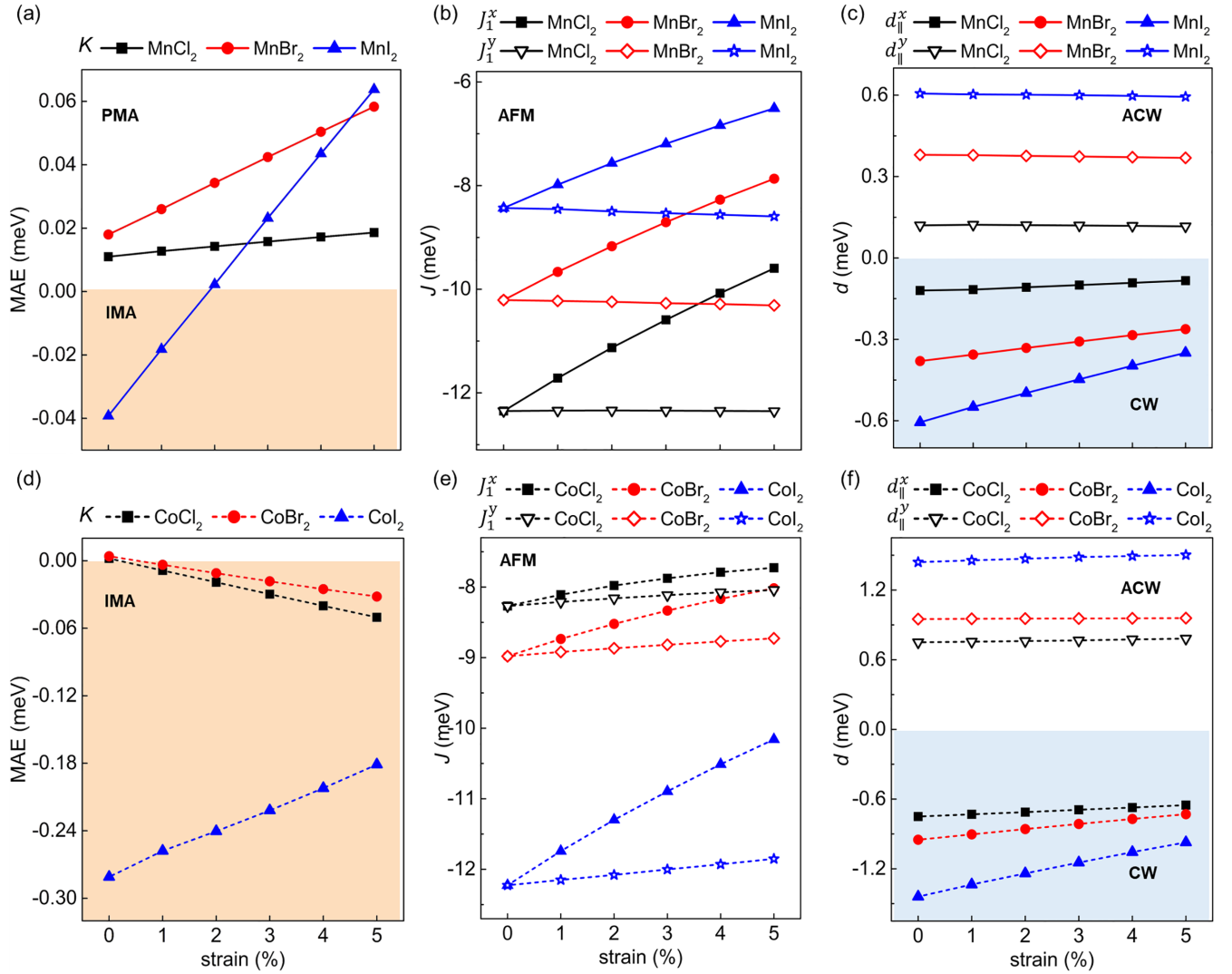


FIG. 3. (a),(d) magnetic anisotropy K ; (b),(e) nearest-neighboring exchange coupling at the x - and y -directions J_1^x and J_1^y ; and (c),(f) in-plane component of DMI between nearest-neighboring magnetic atoms at the x - and y -directions $d_{||}^x$ and $d_{||}^y$ of MnA_2 and CoA_2 ($A = \text{Cl}, \text{Br}, \text{I}$) monolayers under the strain along the x -axis.

downward and the structure is stretched along the y -direction. The angle change of $\angle\text{OBC}$ can be used to describe the deformation mechanism inside the lattice [43,44]. The decreased $\angle\text{OBC}$ upon applying strain further confirms that the strong e - p orbital coupling leads to the NPR effect in the xy plane. On the contrary, the PPR appears in the FeI_2 monolayer due to the weak e - p orbitals coupling between Fe and I atoms (Appendix 1). Thus, the discrepancies between Poisson's ratio of MnCl_2 (CoCl_2) and FeI_2 with the same symmetry confirm that the electronic state is responsible for the NPR behavior in these monolayers.

Unlike the mechanical stability, we demonstrate the dynamic and thermal stability of these auxetic materials by calculating the phonon dispersion and performing *ab initio* molecular dynamics (AIMD). We note that in the calculated phonon band structures of MnCl_2 and CoBr_2 , small acoustic imaginary modes appear around the Γ point, which is interpreted as instability against long-wavelength transverse waves (see Appendix 2). This instability does not significantly affect

the whole structure and the properties of these 2D materials, and it can be eliminated by ripples in the structures. After heating at 500 K for 8 ps with a time step of 1 fs, the variation of potential energy is kept at a small amplitude near the average value during the entire simulation, and all structures are still maintained at the initial phase (see Appendix 2), indicating a good thermal stability of MnA_2 and CoA_2 monolayers. The system energy of auxetic magnets is summarized in Appendix 2 as a function of strains. The strain-induced energy difference compared with the ground state is smaller than 100 meV, thus it is feasible to apply external strain in these auxetic magnets.

B. Tunable topological magnetism

Previous studies have proposed and illustrated a family of 2D magnets MX_2 with $P4m2$ symmetry-protected anisotropic DMI, and various topological spin configurations, including FM/AFM antiskyrmions and AFM vortex-antivortex pairs,

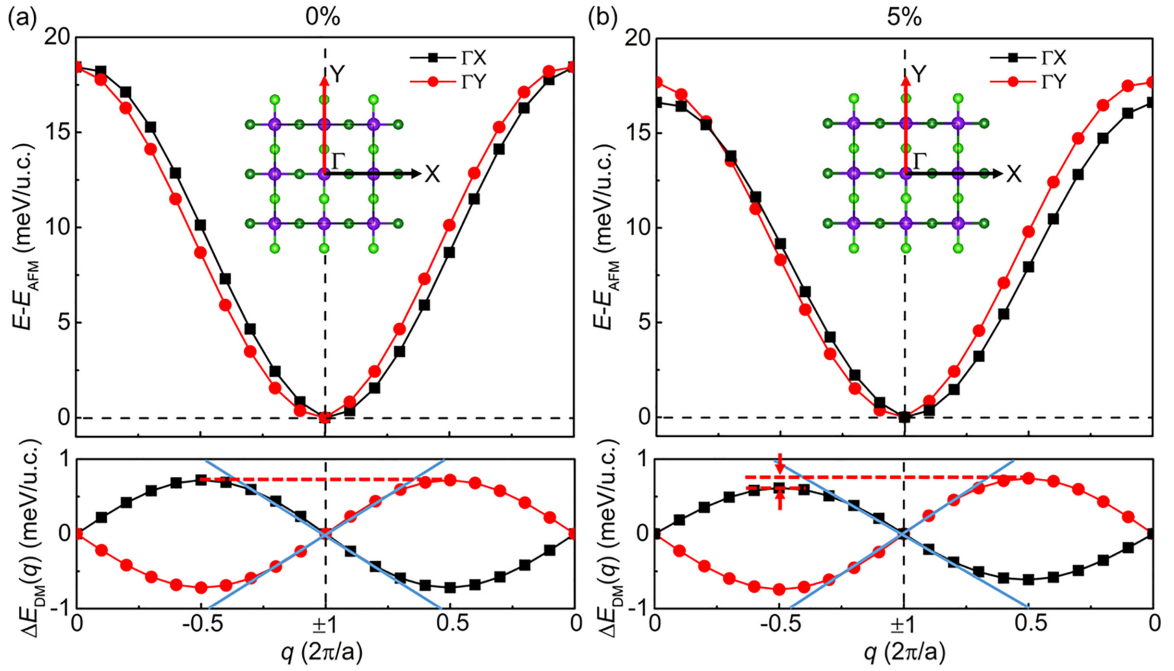


FIG. 4. Calculation of magnetic parameters by the qSO method for CoCl_2 monolayer under (a) 0% and (b) 5% uniaxial tensile strain. Spin spiral energy $E(q)$ (upper panel) and DMI energy $\Delta E_{\text{DM}}(q)$ (lower panel) calculated as a function of spiral vector length q . $E(q)$ is given with respect to the antiferromagnetic state at $q = \pm 1$. Black and red points are calculated with q along with Γ -X and Γ -Y [insets (a) and (b)], respectively. Blue lines in the lower panels in (a) and (b) are linear fits of $\Delta E_{\text{DM}}(q)$, which is based on the atomistic extended spin Hamiltonian. Red dashed lines indicate the strength of the anisotropic DMI $d_{\parallel}^x = -d_{\parallel}^y$ and $d_{\parallel}^x < -d_{\parallel}^y$, which are obtained in CoCl_2 at 0% and 5% strain, respectively.

emerge in these materials [28,45]. As mentioned above, a stronger NPR effect observed in MnA_2 and CoA_2 ($A = \text{Cl, Br, I}$) monolayers means that as the tensile strain is applied in the x -direction, the equilibrium lattice constant

is increased in the y -direction. Notably, the size and density of those chiral spin textures can be tuned through strain engineering [46]. Therefore, we focus on the topological magnetic properties and topological spin textures of

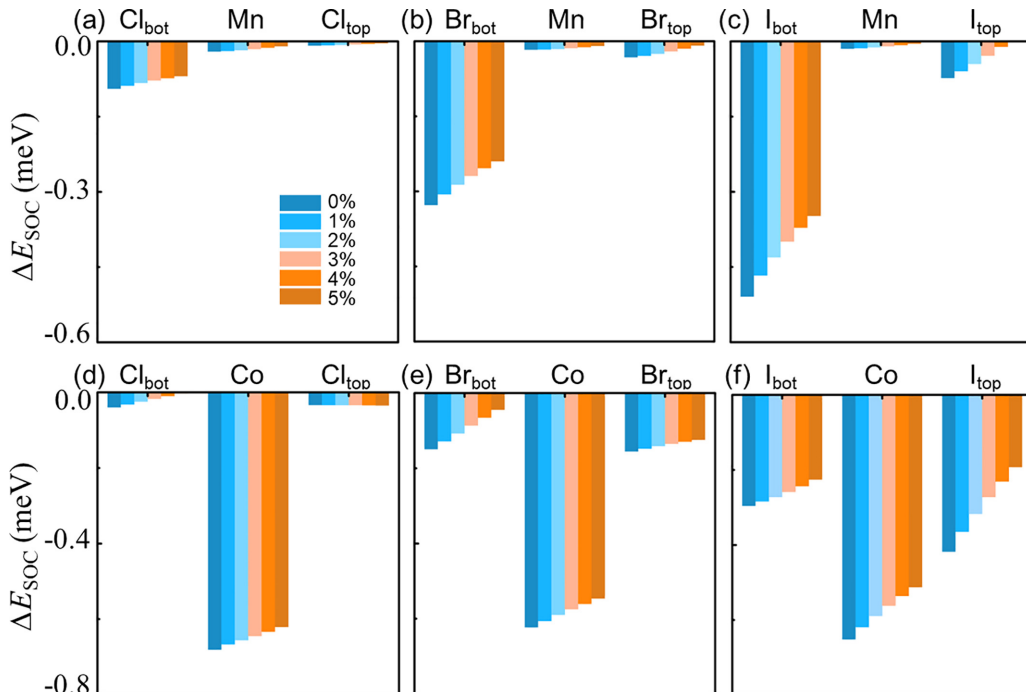


FIG. 5. Atomic-layer-resolved localization of SOC energy difference ΔE_{SOC} for (a)–(c) MnA_2 and (d)–(f) CoA_2 ($A = \text{Cl, Br, I}$) monolayers. ΔE_{SOC} is shown with spin rotating along the x -axis.

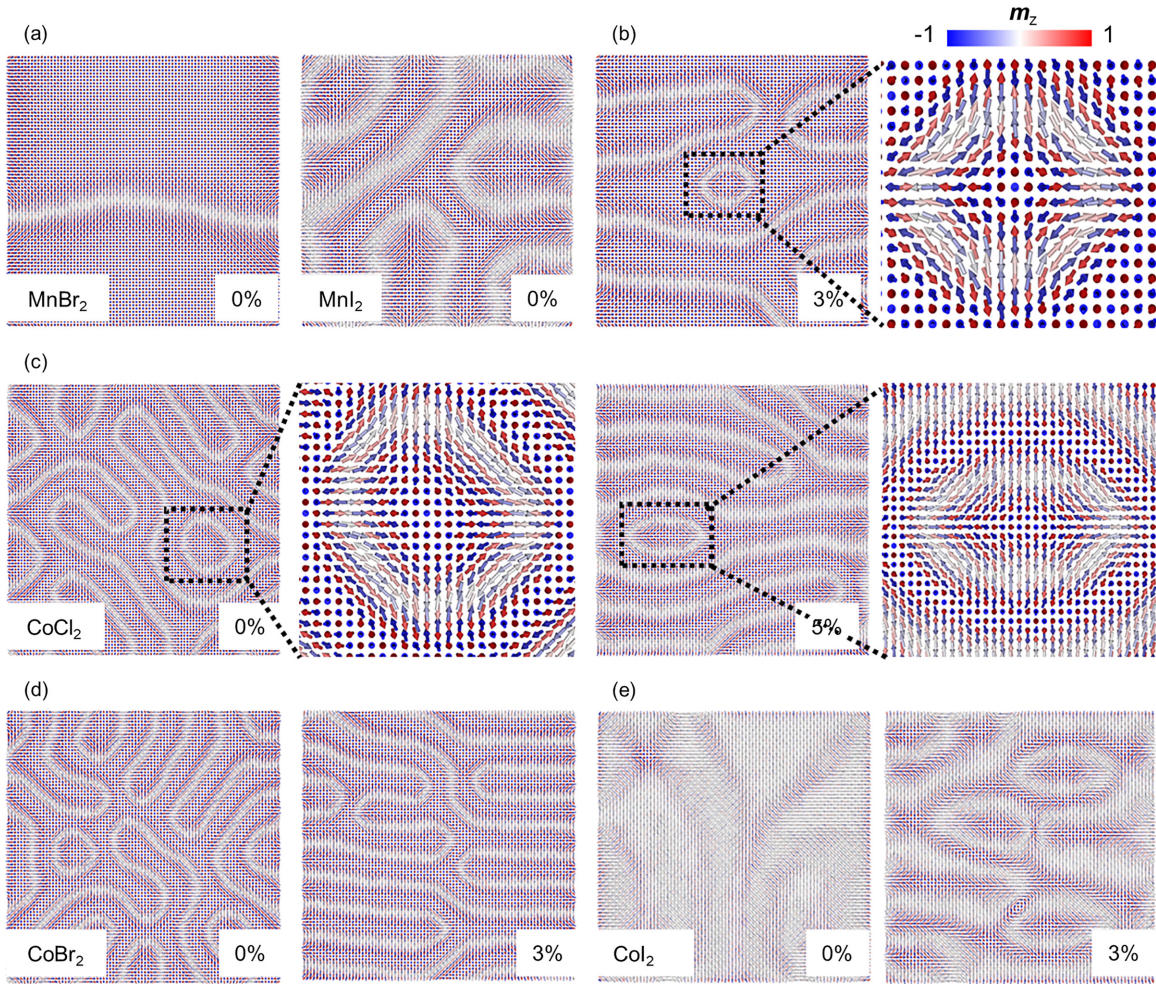


FIG. 6. Real-space spin configurations obtained from atomistic spin model simulations. Spin textures of a $100 \text{ nm} \times 100 \text{ nm}$ square and zooms of a topological quasiparticle (indicated by dashed rectangle) of auxetic materials (a) MnBr_2 , (b) MnI_2 , (c) CoCl_2 , (d) CoBr_2 , and (e) CoI_2 . Uniaxial tensile strain is applied in monolayers. The color map indicates the out-of-plane spin component, and the arrows indicate the orientation of the in-plane spin component.

auxetic materials MnA_2 and CoA_2 under uniaxial tensile strain.

We adopt the following spin Hamiltonian to investigate the magnetic properties of auxetic monolayers of MnA_2 and CoA_2 :

$$H = -K \sum_i (S_i^z)^2 - J_1 \sum_{\langle i,j \rangle} \mathbf{S}_i \cdot \mathbf{S}_j - J_2 \sum_{\langle i',j' \rangle} \mathbf{S}_{i'} \cdot \mathbf{S}_{j'} - \sum_{\langle i,j \rangle} \mathbf{D}_{ij} \cdot (\mathbf{S}_i \times \mathbf{S}_j), \quad (2)$$

where $\mathbf{S}_{i(j)}$ is a unit vector representing the orientation of the spin of the i th (j th) M atom, and $\langle i, j \rangle$ and $\langle i', j' \rangle$ represent the nearest-neighbor (NN) and next-nearest-neighbor (NNN) of M atom pairs, respectively. The magnetic parameters K , J_1 , J_2 , and \mathbf{D}_{ij} in the first three terms represent the magnetic anisotropy, NN, NNN exchange coupling, and interatomic DMI, respectively. The $P4m2$ layer group contains a twofold axis and two mirror symmetries. According to Moriya symmetry rules [24], the sign of the in-plane DMI components should be opposite along the x - and y -directions, $d_{\parallel}^x = -d_{\parallel}^y$, which is indicated in Fig. 1(a). When the uniaxial strain is

applied in the x -direction for MnA_2 and CoA_2 monolayers with NPR, the lattice in the y -direction expands to $a_y - \varepsilon_x \times \nu$, which leads to anisotropic NN exchange coupling. The computational details about these magnetic parameters are illustrated in Appendix 3 and the DFT results are shown in Fig. 3. For magnetic anisotropy energy, $K > 0$ and $K < 0$ indicate perpendicular magnetic anisotropy (PMA) and in-plane magnetic anisotropy (IMA), while for exchange coupling, $J > 0$ and $J < 0$ indicate the FM and AFM coupling, respectively. In pristine MnCl_2 , MnBr_2 , and CoI_2 monolayers, the direction of magnetic anisotropy can be maintained, while the IMA-to-PMA transition is observed in MnI_2 , CoCl_2 , and CoBr_2 monolayers under external strain. MnA_2 and CoA_2 monolayers prefer AFM exchange coupling, where the NN exchange coupling in the x -direction (J_1^x) decreases with the increase of the uniaxial strain, while it has little change along the y -direction (J_1^y). The NNN exchange coupling J_2 is isotropic, and its strength is much smaller than J_1 . For the calculated DMI, the in-plane (IP) DMI components $d_{\parallel}^{x(y)} > 0$ and $d_{\parallel}^{x(y)} < 0$ favor an anticlockwise (ACW) and clockwise (CW) spin configuration, respectively. As required by the symmetry

TABLE II. The magnetic anisotropy (K), nearest-neighboring at the x - and y -directions and next-nearest-neighboring exchange coupling (J_1^x , J_1^y , and J_2), and in-plane component of DMI between nearest-neighboring magnetic atoms d_{\parallel}^x and d_{\parallel}^y of CoCl_2 monolayer with and without the NPR effect when 5% tensile strain is applied along the x - and y -axis. The unit of K is meV/atom; the units of J_1^x , J_1^y , and J_2 are meV; and the units of d_{\parallel}^x and d_{\parallel}^y are meV.

		K	J_1^x	J_1^y	J_2	d_{\parallel}^x	d_{\parallel}^y
y-direction	with NPR	-0.050	8.042	7.726	0.171	-0.782	0.652
x-direction	with NPR	-0.050	7.726	8.042	0.171	-0.652	0.782
	without NPR	-0.052	7.729	8.101	0.181	-0.625	0.767

feature, the out-of-plane (OOP) DMI component d_{\perp}^z vanishes due to the M - X - M in one mirror plane. Apparently, the DMI in the x - and y -directions favors CW and ACW chirality, respectively. Remarkably, the amplitudes of d_{\parallel}^x and d_{\parallel}^y are modulated by uniaxial strain, which results in an unequal strength of DMI along different axial directions. In addition, to demonstrate the reliability of the results obtained from the chirality-dependent energy difference (CDED) approach, we adapt the qSO method, in which the SOC is considered in first-order perturbation theory using a self-consistent method to calculate $E(\mathbf{q})$. $E(\mathbf{q})$ represents the energy functional of a spin spiral for MX_2 monolayers, where q is the spiral length, and the DMI energy can be calculated as $\Delta E_{\text{DM}}(\mathbf{q}) = [E(\mathbf{q}) - E(-\mathbf{q})]/2$ (see Appendix 3). As shown in Fig. 4, we take a $2 \times 2 \times 1$ CoCl_2 supercell with 0% and 5% uniaxial tensile strain as an example to compare the difference between the DMI in auxetic materials in the x - and y -directions, which correspond to the ΓX and ΓY directions in the Brillouin zone of reciprocal space [see the inset of Figs. 4(a) and 4(b)]. From the spin spiral energy $E(\mathbf{q})$ shown in the upper panel of Fig. 4, CW and ACW rotating is favored when \mathbf{q} is along the ΓX and ΓY directions, respectively, demonstrating the anisotropic feature of DMI. The calculated $\Delta E_{\text{DM}}(\mathbf{q})$ shows a good linear dependence on q close to the Γ point, and d_{\parallel}^x and d_{\parallel}^y of pristine CoCl_2 is -0.696 and 0.696 meV, respectively [see the lower panel in Fig. 4(a)]. When the 5% uniaxial tensile strain is applied in CoCl_2 , the chirality of the spin spiral remains opposite in the ΓX and ΓY directions, while the magnitude of DMI becomes unequal along the x - and y -axis, indicated by the different d_{\parallel}^x and d_{\parallel}^y of -0.629 and 0.721 meV, respectively, according to the linear fit of $\Delta E_{\text{DM}}(\mathbf{q})$ [see the lower panel in Fig. 4(b)]. The details on the computational method of $d_{\parallel}^{x(y)}$ are explained in Appendix 3. These values indicate that the calculated DMI using the CDED approach are in agreement with the qSO method.

We further calculate the layer-resolved SOC energy difference ΔE_{SOC} between CW and ACW spin configurations with rotation along the x -direction to elucidate the origin of DMI in NPR materials (see Fig. 5). Actually, the calculated ΔE_{SOC} shows opposite chirality in the x - and y -directions, and it can be modified under the uniaxial strain along the x -direction. In MnA_2 and CoA_2 monolayers, the largest value of ΔE_{SOC} originates from A_{bot} and Co layer, respectively. These features indicate that the physical mechanism governing the strength of the DMI in MnA_2 and CoA_2 monolayers is consistent with the Fert-Levy model and Rashba-type interaction, respectively [37,47]. We also notice that the contribution of DMI from the A layer keeps increasing as the SOC strength of A is enhanced

(from Cl to I). The decay of ΔE_{SOC} with the increase of strain reflects the variation of d_{\parallel}^x .

Once all the magnetic parameters with the NPR effect in the spin Hamiltonian are calculated, we can perform the atomistic spin model simulations (see Fig. 6) of auxetic materials using the VAMPIRE package in a large enough space with a square length of 100 nm [48]. The initial spin direction is set to random states in the open boundary. The uniform antiferromagnetic background emerges in the MnCl_2 monolayer depending on a weak DMI strength, and it cannot be changed under external strain. Compared with MnCl_2 , the NN exchange coupling decreases while the DMI largely increases in MnBr_2 and MnI_2 monolayers, resulting in the existence of a domain wall in the PMA and IMA systems, respectively. With the IMA-to-PMA transition and the decrease of K , the elliptical AFM antiskyrmion ($r_x/r_y = 1.48$) is embedded in the domain for MnI_2 under 3% tensile strain. In the pristine CoCl_2 to CoI_2 transition, AFM antiskyrmion and vortices are observed, which is a result of a much stronger DMI (d_{\parallel}^y) compared with magnetic anisotropy and exchange coupling. Interestingly, the AFM antiskyrmion in pristine CoCl_2 is elongated to be transverse elliptical ($r_x/r_y = 2.40$) as strain increases to 5% along the x -axis. When 5% strain is applied along the y -axis, d_{\parallel}^x is greater than d_{\parallel}^y (Table II), and the longitudinal elliptical AFM antiskyrmion with $r_x/r_y = 0.64$ can be stabilized in CoCl_2 (Appendix 4). Similarly, elliptical skyrmions have been observed experimentally in the single-crystal film FeGe [49] and asymmetric magnetic multilayer Pt/Co/Ta [50], which is correlated to the perpendicular

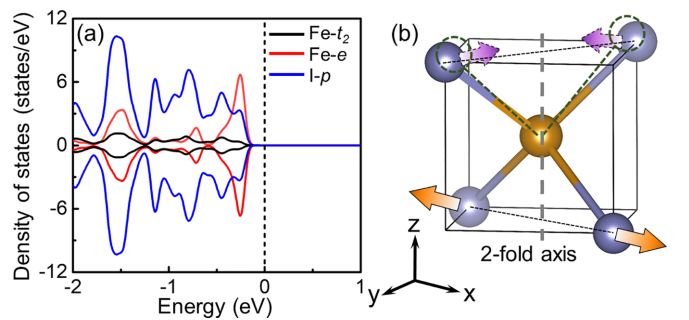


FIG. 7. (a) Atom-projected density of states, and (b) schematic diagram of the geometric evolution for FeI_2 . Black, red, and blue lines represent the t_2 (d_{xy} , d_{xz} , d_{yz}) and e ($d_{x^2-y^2}$, d_{z^2}) orbitals of metal atoms and p -orbitals of nonmagnetic elements, respectively. Purple arrows in (b) indicate the resulting movement of the l_{top} atom under a tensile strain along the x -axis.

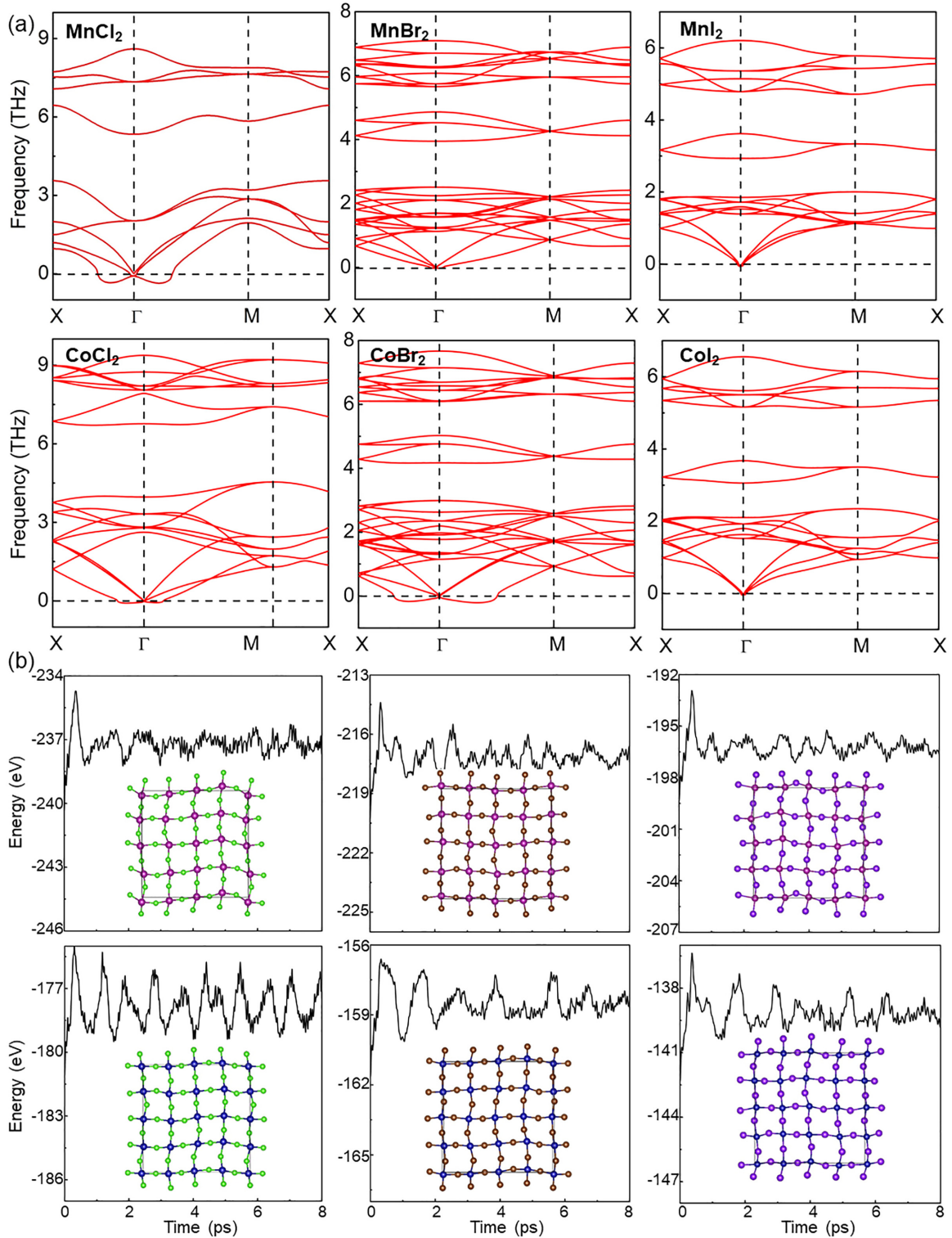


FIG. 8. (a) Calculated phonon band structure for MnA_2 and CoA_2 ($A = \text{Cl, Br, I}$) monolayers. (b) The evolution of the total internal energy and structural snapshots after 8 ps during *ab initio* MD simulations for MnA_2 and CoA_2 ($A = \text{Cl, Br, I}$) monolayers at 500 K.

magnetic anisotropy and anisotropic DMI strength. Furthermore, to demonstrate the necessity of mechanical properties in those 2D magnets, we compare the magnetic parameters of CoCl_2 with and without considering the NPR effect under 5% tensile strain along the x -axis, and the results are listed in Table II. Obviously, the exchange coupling J_1^y of CoCl_2 in-

creases and the strength of DMI decreases when the NPR effect is not considered, which leads to a meandering domain instead of the elliptical antiferromagnetic antiskyrmion, as shown in Appendix 4. The clear distinction between topological spin configurations shows that the NPR plays an important role and cannot be neglected in MnA_2 and CoA_2 monolayers.

Thus, the coexistence of anisotropic DMI and the NPR effect in MnI_2 and CoCl_2 monolayers leads to the formation of elliptical antiferromagnetic antiskyrmions under uniaxial strain.

IV. CONCLUSION

In summary, we propose a series of two-dimensional antiferromagnetic compounds with $P4m2$ crystal symmetry, MnA_2 and CoA_2 ($A = \text{Cl}, \text{Br}, \text{I}$), with a large negative Poisson ratios. The auxetic behavior is mainly dependent on the hybridization between d -orbitals of metal atoms and p -orbitals of nonmagnetic atoms. We further find that the absolute value of anisotropic DMI along x - and y -axis can be modulated by uniaxial strain under the influence of the NPR effect, resulting in the appearance of an elliptical antiferromagnetic antiskyrmion. The advantages of strain tunability, flexibility, and miniaturization of these auxetic magnets can be used to achieve unexpected topological magnetism and to design skyrmionic devices with a simpler structure and higher efficiency. Our work explores 2D auxetic materials with intrinsic long-range magnetic order and anisotropic DMI, which provide a platform for designing topological chiral textures.

ACKNOWLEDGMENTS

This work was supported by the ‘‘Pioneer’’ and ‘‘Leading Goose’’ R&D Program of Zhejiang Province (Grant No. 2022C01053), National Key Research and Development Program of China (MOST) (Grant No. 2022YFA1405100), and the National Natural Science Foundation of China (Grants No. 12174405 and No. 12204497).

APPENDIX

1. DOS and geometric evolution of FeI_2 with large PPR

We calculate the density of states of FeI_2 monolayer with large PPR as a comparison to clarify the mechanism of Poisson’s ratio, as shown in Fig. 7. One can see that the e - p orbital coupling is obviously weaker than the MnCl_2 and CoCl_2 monolayers in the $[-1, 0]$ energy range. The magnetic atom is not subjected to compressive force in the z -direction, therefore the structure will not be compressed in the z -direction and stretched in the y -direction.

2. Phonon calculation, molecular dynamics, and external strain adjustability

To verify the dynamics and thermal stability of MnA_2 and CoA_2 ($A = \text{Cl}, \text{Br}, \text{I}$) monolayers, we perform phonon dispersions and *ab initio* molecular dynamics implemented in VASP. The real-space force constants are computed with a large supercell (either $4 \times 4 \times 1$ or $3\sqrt{2} \times 3\sqrt{2} \times 1$) using the PHONOPY code [35]. For an NVT (N is the number of particles, V is the volume, and T is the temperature) ensemble, a $4 \times 4 \times 1$ supercell with a $1 \times 1 \times 1$ k -point grid is adopted [36]. Figure 8 shows the phonon band structure and the evolution of the total energy of these systems. The system energy of auxetic magnets is summarized in Fig. 9 as a function of strains. When the uniaxial strains are applied, the energy difference between the system and ground state is smaller

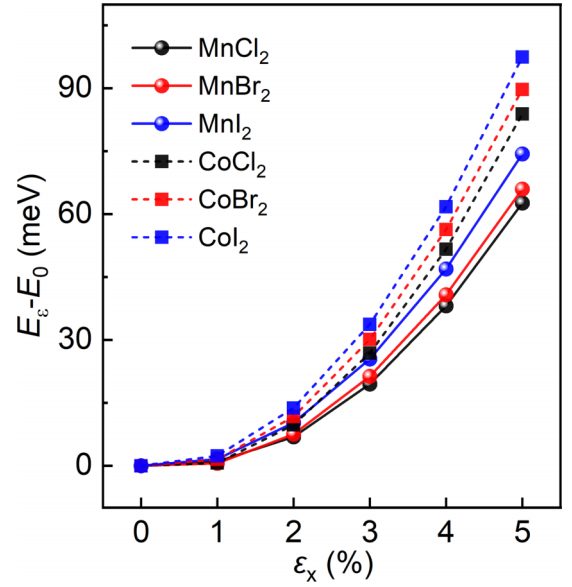


FIG. 9. The energy variation in auxetic magnets MnA_2 and CoA_2 as a function of different uniaxial tensile strains.

than 100 meV, which indicates that it is feasible to apply the external strain in these auxetic magnets.

3. Calculations of K , J , and d_{\parallel}

(i) The magnetic anisotropy K is obtained by $K = E_{100} - E_{001}$, where E_{100} and E_{001} represent the total energy with magnetization along the positive direction of the x - and z -axis, respectively. (ii) To calculate the nearest-neighbor (NN) in the x - and y -directions (J_1^x and J_1^y), and next-nearest-neighbor

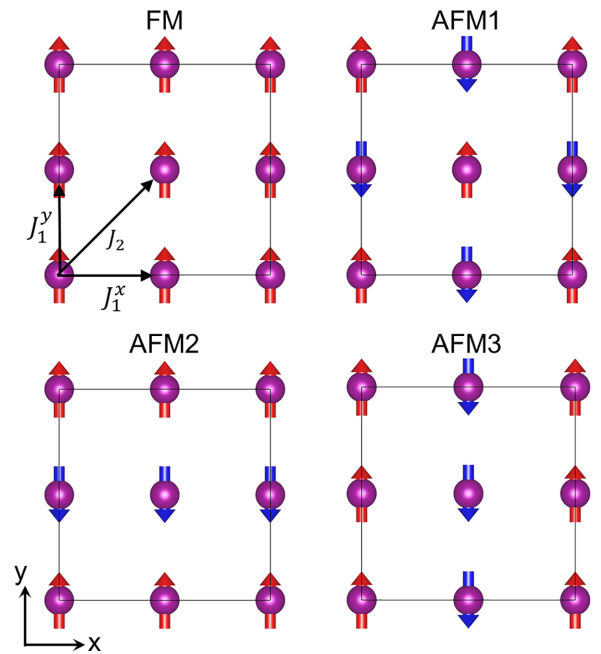


FIG. 10. Four spin configurations (FM, G-type AFM, vertical stripe-type AFM, and horizontal stripe-type AFM) of a $2 \times 2 \times 1$ supercell applied to calculate the nearest-neighboring (J_1^x and J_1^y) and next-nearest-neighboring (J_2) exchange coupling parameters.

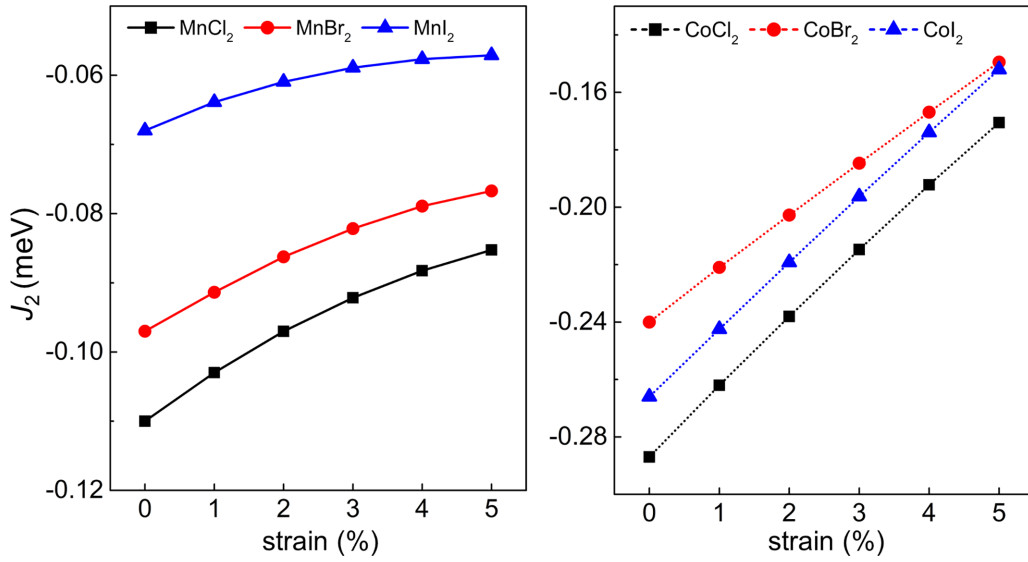


FIG. 11. The next-nearest-neighbor exchange coupling J_2 of MnA_2 and CoA_2 ($A = Cl, Br, I$) monolayers.

(NNN) exchange coupling (J_2), the DFT total energy difference of four spin configurations, including FM, G-type AFM, vertical stripe-type AFM, and horizontal stripe-type AFM, is calculated in a $2 \times 2 \times 1$ supercell (Fig. 10). The total energies of these configurations are given by

$$\begin{aligned}
 E_{\text{FM}} &= -4J_1^x - 4J_1^y - 8J_2 + E_0, \\
 E_{\text{AFM1}} &= 4J_1^x + 4J_1^y - 8J_2 + E_0, \\
 E_{\text{AFM2}} &= 4J_1^x - 4J_1^y + 8J_2 + E_0, \\
 E_{\text{AFM3}} &= -4J_1^x + 4J_1^y + 8J_2 + E_0.
 \end{aligned} \quad (\text{A1})$$

J_1^x , J_1^y , and J_2 are written as

$$\begin{aligned}
 J_1^x &= \frac{-E_{\text{FM}} + E_{\text{AFM1}} + E_{\text{AFM2}} - E_{\text{AFM3}}}{16}, \\
 J_1^y &= \frac{-E_{\text{FM}} + E_{\text{AFM1}} - E_{\text{AFM2}} + E_{\text{AFM3}}}{16}, \\
 J_2 &= \frac{-E_{\text{FM}} - E_{\text{AFM1}} + E_{\text{AFM2}} + E_{\text{AFM3}}}{32}.
 \end{aligned} \quad (\text{A2})$$

The calculated NNN exchange coupling of MnA_2 and CoA_2 ($A = Cl, Br, I$) monolayers is shown in Fig. 11. (iii) In calculations of the in-plane component of DMI strength d_{\parallel}^x (d_{\parallel}^y), a $4 \times 1 \times 1$ ($1 \times 4 \times 1$) supercell and a Γ -centered $4 \times 16 \times 1$ ($16 \times 4 \times 1$) k -point mesh is adopted. We calculate the chirality-dependent energy difference (CDED) between the clockwise $\{(0\ 0\ S), (S\ 0\ 0), (00\ -S), (-S00)\}$ and anticlockwise $\{(00S), (-S00), (00\ -S), (00S)\}$ energy chirality with SOC effects to obtain d_{\parallel} , $d_{\parallel} = (E_{\text{cw}} - E_{\text{acw}})/8$. (iv) To calculate the magnetic parameters by the qSO method, the spin Hamiltonian for 2D magnets is

$$H = -K \sum_i (\mathbf{m}_i^z)^2 - J_{ij} \sum_{\langle i,j \rangle} \mathbf{m}_i \cdot \mathbf{m}_j - \sum_{\langle i,j \rangle} \mathbf{D}_{ij} \cdot (\mathbf{m}_i \times \mathbf{m}_j), \quad (\text{A3})$$

where $\mathbf{m}_{i(j)}$ is the unit magnetization vector at position $\mathbf{r}_{i(j)}$. The DFT energy of a noncollinear homogeneous spin spiral $\mathbf{m} = (\sin(\mathbf{q} \cdot \mathbf{r}), 0, \cos(\mathbf{q} \cdot \mathbf{r}))$, with \mathbf{q} being a spin spiral vector, is calculated to obtain the in-plane component of \mathbf{D}_{ij} .

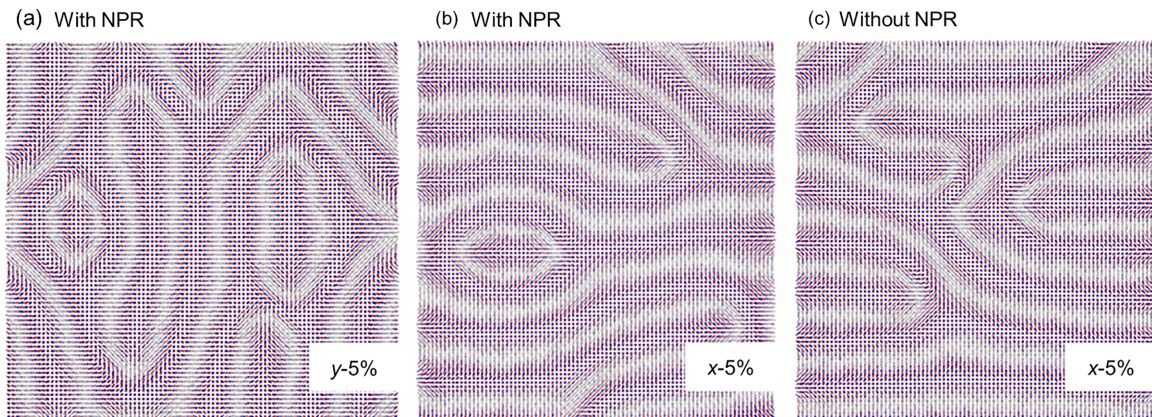


FIG. 12. Real-space spin configurations of $CoCl_2$ with a negative Poisson ratio effect when the 5% tensile strain is along the (a) y -axis and (b) x -axis, and (c) without NPR when the strain is applied along the x -axis.

Then the system energy functional of \mathbf{q} is

$$E(\mathbf{q}) = -K \sum_i [\cos(\mathbf{q} \cdot \mathbf{r}_i)]^2 - J_{ij} \sum_{(i,j)} \cos(\mathbf{q} \cdot (\mathbf{r}_j - \mathbf{r}_i)) - \sum_{(i,j)} D_y \sin(\mathbf{q} \cdot (\mathbf{r}_j - \mathbf{r}_i)). \quad (\text{A4})$$

Therefore, we can identify the DMI energy as

$$\Delta E_{\text{DM}}(\mathbf{q}) = \frac{E(\mathbf{q}) - E(-\mathbf{q})}{2} = \sum_{(i,j)} D_{x(y)} \sin[\mathbf{q} \cdot (\mathbf{r}_j - \mathbf{r}_i)], \quad (\text{A5})$$

where $D_{x(y)} > 0$ ($D_{x(y)} < 0$) favors an ACW (CW) spin configuration. When \mathbf{q} is along ΓX and ΓY of a $2 \times 2 \times 1$ supercell and its magnitude q is close to 0 or ± 1 , the relationship between $\Delta E_{\text{DM}}(q)$ and q is $\Delta E_{\text{DM}}(q) \propto D_{x(y)} q$. The spin spirals that propagate along the NN magnetic atoms in the x - and y -directions are shown in inset of Fig. 4(a). The $d_{\parallel}^{x(y)}$ can be calculated as $d_{\parallel}^{x(y)} = \frac{D_{x(y)}}{2r}$, where r represents

the lattice constant of a supercell. In our calculations, the generalized Bloch theorem and spin-orbit coupling within the first-order perturbation theory are employed. The full SOC operator H_{SOC} determined by its component along the rotation axis of the spiral, which is $H_{\text{SOC}}^{x(y)}$, is considered to include SOC effects in a self-consistent way. We perform the qSO method in conjunction with the VASP package.

4. Simulations of CoCl_2 under the external strain with and without NPR

All atomic spin model simulations are performed using the VAMPIRE package [48], which is extended to a $100 \text{ nm} \times 100 \text{ nm}$ square with open boundaries. Figures 12(b) and 12(c) illustrate the importance of considering the NPR in these monolayers. Furthermore, the uniaxial strain is along the y -direction, the magnetic parameters are shown in Table II, and the elliptical AFM antiskyrmion can also be induced in CoCl_2 monolayers [Fig. 12(a)].

-
- [1] L. D. Landau and E. M. Lifshitz, *Theory of Elasticity* (Pergamon, Oxford, 1995).
- [2] K. E. Evans, M. A. Nkansah, I. J. Hutchinson, and S. C. Rogers, Molecular network design, *Nature (London)* **353**, 124 (1991).
- [3] M. Avellaneda and P. J. Swart, Calculating the performance of 1–3 piezoelectric composites for hydrophone applications: An effective medium approach, *J. Acoust. Soc. Am.* **103**, 1449 (1998).
- [4] J. Choi and R. Lakes, Design of a fastener based on negative Poisson's ratio foam, *Cell. Polym.* **10**, 205 (1991).
- [5] F. Scarpa, Auxetic materials for bioprotheses [In the Spotlight], *IEEE Sign. Process. Mag.* **25**, 128 (2008).
- [6] R. C. Andrew, R. E. Mapasha, A. M. Ukpogon, and N. Chetty, Mechanical properties of graphene and boronitrene, *Phys. Rev. B* **85**, 125428 (2012).
- [7] S. Guo and H. Sun, Manipulation of giant negative Poisson's ratios in three-dimensional graphene networks, *Phys. Rev. B* **102**, 184116 (2020).
- [8] R. Lakes, Advances in negative Poisson's ratio materials, *Adv. Mater.* **5**, 293 (1993).
- [9] J. W. Jiang, T. Chang, X. Guo, and H. S. Park, Intrinsic negative Poisson's ratio for single-layer graphene, *Nano Lett.* **16**, 5286 (2016).
- [10] S. Zhang, J. Zhou, Q. Wang, X. Chen, Y. Kawazoe, and P. Jena, Penta-graphene: A new carbon allotrope, *Proc. Natl. Acad. Sci. (USA)* **112**, 2372 (2015).
- [11] Z. Gao, X. Dong, N. Li, and J. Ren, Novel two-dimensional silicon dioxide with in-plane negative Poisson's ratio, *Nano Lett.* **17**, 772 (2017).
- [12] P. Jiang, L. Kang, X. Zheng, Z. Zeng, and S. Sanvito, Computational prediction of a two-dimensional semiconductor SnO_2 with negative Poisson's ratio and tunable magnetism by doping, *Phys. Rev. B* **102**, 195408 (2020).
- [13] J. W. Jiang and H. S. Park, Negative Poisson's ratio in single-layer black phosphorus, *Nat. Commun.* **5**, 4727 (2014).
- [14] J. Pan, Y. F. Zhang, J. Zhang, H. Banjade, J. Yu, L. Yu, S. Du, A. Ruzsinszky, Z. Hu, and Q. Yan, Auxetic two-dimensional transition metal selenides and halides, *npj Comput. Mater.* **6**, 1 (2020).
- [15] S. Heinze, K. von Bergmann, M. Menzel, J. Brede, A. Kubetzka, R. Wiesendanger, G. Bihlmayer, and S. Blügel, Spontaneous atomic-scale magnetic skyrmion lattice in two dimensions, *Nat. Phys.* **7**, 713 (2011).
- [16] J. Sampaio, V. Cros, S. Rohart, A. Thiaville, and A. Fert, Nucleation, stability and current-induced motion of isolated magnetic skyrmions in nanostructures, *Nat. Nanotechnol.* **8**, 839 (2013).
- [17] B. Göbel, A. Mook, J. Henk, I. Mertig, and O. A. Tretiakov, Magnetic bimerons as skyrmion analogues in in-plane magnets, *Phys. Rev. B* **99**, 060407(R) (2019).
- [18] J. Barker and O. A. Tretiakov, Static and dynamical properties of antiferromagnetic skyrmions in the presence of applied current and temperature, *Phys. Rev. Lett.* **116**, 147203 (2016).
- [19] X. Zhang, Y. Zhou, and M. Ezawa, Antiferromagnetic skyrmion: Stability, creation and manipulation, *Sci. Rep.* **6**, 24795 (2016).
- [20] R. Msiska, D. R. Rodrigues, J. Leliaert, and K. Everschor-Sitte, Nonzero skyrmion Hall effect in topologically trivial structures, *Phys. Rev. Appl.* **17**, 064015 (2022).
- [21] J. Spethmann, M. Grünebohm, R. Wiesendanger, K. von Bergmann, and A. Kubetzka, Discovery and characterization of a new type of domain wall in a row-wise antiferromagnet, *Nat. Commun.* **12**, 3488 (2021).
- [22] H. Jani, J. C. Lin, J. Chen, J. Harrison, F. Maccherozzi, J. Schäd, S. Prakash, C. B. Eom, A. Ariando, T. Venkatesan, and P. G. Radaelli, Antiferromagnetic half-skyrmions and bimerons at room temperature, *Nature (London)* **590**, 74 (2021).
- [23] I. Dzyaloshinsky, A thermodynamic theory of "weak" ferromagnetism of antiferromagnetics, *J. Phys. Chem. Solids* **4**, 241 (1958).
- [24] T. Moriya, Anisotropic superexchange interaction and weak ferromagnetism, *Phys. Rev.* **120**, 91 (1960).
- [25] A. Fert and P. M. Levy, Role of anisotropic exchange interactions in determining the properties of spin-glasses, *Phys. Rev. Lett.* **44**, 1538 (1980).

- [26] S. Hastrup, M. Strange, M. Pandey, T. Deilmann, P. S. Schmidt, N. F. Hinsche, M. N. Gjerding, D. Torelli, P. M. Larsen, A. C. Riis-Jensen, J. Gath, K. W. Jacobsen, J. J. Mortensen, T. Olsen, and K. S. Thygesen, The Computational 2D Materials Database: High-throughput modeling and discovery of atomically thin crystals, *2D Mater.* **5**, 042002 (2018).
- [27] M. N. Gjerding, A. Taghizadeh, A. Rasmussen, S. Ali, F. Bertoldo, T. Deilmann, N. R. Knøsgaard, M. Kruse, A. H. Larsen, S. Manti, T. G. Pedersen, U. Petralanda, T. Skovhus, M. K. Svendsen, J. J. Mortensen, T. Olsen, and K. S. Thygesen, Recent progress of the computational 2D materials database (C2DB), *2D Mater.* **8**, 044002 (2021).
- [28] Q. Cui, Y. Zhu, Y. Ga, J. Liang, D. Yu, P. Cui, and H. Yang, Anisotropic Dzyaloshinskii–Moriya interaction and topological magnetism in two-dimensional magnets protected by $P\bar{4}m2$ crystal symmetry, *Nano Lett.* **22**, 2334 (2022).
- [29] G. Kresse and J. Hafner, Ab initio molecular dynamics for liquid metals, *Phys. Rev. B* **47**, 558 (1993).
- [30] G. Kresse and J. Hafner, Ab initio molecular-dynamics simulation of the liquid-metal–amorphous-semiconductor transition in germanium, *Phys. Rev. B* **49**, 14251 (1994).
- [31] G. Kresse and J. Furthmüller, Efficiency of ab-initio total energy calculations for metals and semiconductors using a plane-wave basis set, *J. Comput. Mater. Sci.* **6**, 15 (1996).
- [32] P. E. Blöchl, Projector augmented-wave method, *Phys. Rev. B* **50**, 17953 (1994).
- [33] J. P. Perdew, K. Burke, and M. Ernzerhof, Generalized gradient approximation made simple, *Phys. Rev. Lett.* **77**, 3865 (1996).
- [34] G. Kresse and D. Joubert, From ultrasoft pseudopotentials to the projector augmented-wave method, *Phys. Rev. B* **59**, 1758 (1999).
- [35] A. Togo and I. Tanaka, First principles phonon calculations in materials science, *Scr. Mater.* **108**, 1 (2015).
- [36] S. Nosé, A unified formulation of the constant temperature molecular dynamics methods, *J. Chem. Phys.* **81**, 511 (1984).
- [37] H. Yang, A. Thiaville, S. Rohart, A. Fert, and M. Chshiev, Anatomy of Dzyaloshinskii–Moriya interaction at Co/Pt interfaces, *Phys. Rev. Lett.* **115**, 267210 (2015).
- [38] L. M. Sandratskii, Insight into the Dzyaloshinskii–Moriya interaction through first-principles study of chiral magnetic structures, *Phys. Rev. B* **96**, 024450 (2017).
- [39] M. Heide, G. Bihlmayer, and S. Blügel, Describing Dzyaloshinskii–Moriya spirals from first principles, *Physica B* **404**, 2678 (2009).
- [40] R. Qin, C. H. Wang, W. Zhu, and Y. Zhang, First-principles calculations of mechanical and electronic properties of silicene under strain, *AIP Adv.* **2**, 022159 (2012).
- [41] R. John and B. Merlin, Theoretical investigation of structural, electronic, and mechanical properties of two-dimensional C, Si, Ge, Sn, *Cryst. Struct. Theory Appl.* **5**, 43 (2016).
- [42] L. Tao, C. Yang, L. Wu, L. Han, Y. Song, S. Wang *et al.*, Tension-induced mechanical properties of stanene, *Mod. Phys. Lett. B* **30**, 1650146 (2016).
- [43] L. Yu, Q. Yan, and A. Ruzsinszky, Negative Poisson’s ratio in 1T-type crystalline two-dimensional transition metal dichalcogenides, *Nat. Commun.* **8**, 1 (2017).
- [44] W. Jin, W. Sun, X. Kuang, C. Lu, and L. Kou, Negative poisson ratio in two-dimensional tungsten nitride: Synergistic effect from electronic and structural properties, *J. Phys. Chem. Lett.* **11**, 9643 (2020).
- [45] Q. Cui, L. Wang, Y. Zhu, J. Liang, and H. Yang, Magnetic anisotropy, exchange coupling and Dzyaloshinskii–Moriya interaction of two-dimensional magnets, *Front. Phys.* **18**, 13602 (2023).
- [46] Q. Cui, J. Liang, Z. Shao, P. Cui, and H. Yang, Strain-tunable ferromagnetism and chiral spin textures in two-dimensional Janus chromium dichalcogenides, *Phys. Rev. B* **102**, 094425 (2020).
- [47] H. Yang, G. Chen, A. A. C. Cotta, A. T. N’Diaye, S. A. Nikolaev, E. A. Soares, W. A. A. Macedo, K. Liu, A. K. Schmid, A. Fert, and M. Chshiev, Significant Dzyaloshinskii–Moriya interaction at graphene–ferromagnet interfaces due to the Rashba effect, *Nat. Mater.* **17**, 605 (2018).
- [48] R. F. Evans, W. J. Fan, P. Chureemart, T. A. Ostler, M. O. A. Ellis, and R. W. Chantrell, Atomistic spin model simulations of magnetic nanomaterials, *J. Phys. Condens. Matter* **26**, 103202 (2014).
- [49] K. Shibata, J. Iwasaki, N. Kanazawa, S. Aizawa, T. Tanigaki, M. Shirai, T. Nakajima, M. Kubota, M. Kawasaki, H. S. Park, D. Shindo, N. Nagaosa, and Y. Tokura, Large anisotropic deformation of skyrmions in strained crystal, *Nat. Nanotech.* **10**, 589 (2015).
- [50] B. Cui, D. Yu, Z. Shao, Y. Liu, H. Wu, P. Nan, Z. Zhu, C. Wu, T. Guo, P. Chen, H. A. Zhou, L. Xi, W. Jiang, H. Wang, S. Liang, H. Du, K. L. Wang, W. Wang, K. Wu, X. Han, G. Zhang, H. Yang, and G. Yu, Néel-type elliptical skyrmions in a laterally asymmetric magnetic multilayer, *Adv. Mater.* **33**, 2006924 (2021).